Equilibrium Gold Nanoclusters Quenched with Biodegradable Polymers

Avinash K. Murthy,[†] Robert J. Stover,[†] Ameya U. Borwankar,[†] Golay D. Nie,[†] Sai Gourisankar,[†] Thomas M. Truskett,[†] Konstantin V. Sokolov,[‡,§] and Keith P. Johnston[†,*]

[†]McKetta Department of Chemical Engineering and [‡]Department of Biomedical Engineering, University of Texas at Austin, Austin, Texas 78712, United States and [§]Department of Imaging Physics, The UT M.D. Anderson Cancer Center, Houston, Texas 77030, United States

ABSTRACT Although sub-100 nm nanoclusters of metal nanoparticles are of interest in many fields including biomedical imaging, sensors, and catalysis, it has been challenging to control their morphologies and chemical properties. Herein, a new concept is presented to assemble equilibrium Au nanoclusters of controlled size by tuning the colloidal interactions with a polymeric stabilizer, PLA(1k)-*b*-PEG(10k)-*b*-PLA(1k). The nanoclusters form upon mixing a dispersion of ~5 nm Au nanospheres with a polymer solution followed by partial solvent evaporation. A weakly adsorbed polymer quenches the equilibrium nanocluster size and provides steric stabilization. Nanocluster size is tuned from ~20 to ~40 nm by experimentally varying the final Au nanoparticle concentration and the polymer/Au ratio, along with the charge on the initial Au nanoparticle surface. Upon biodegradation of the quencher, the nanoclusters reversibly and fully dissociate to individual ~5 nm primary particles. Equilibrium cluster size is predicted semiquantitatively with a free energy model that balances short-ranged depletion and van der Waals attractions with longer-ranged electrostatic repulsion, as a function of the Au and polymer concentrations. The close spacings of the Au nanoparticles in the clusters produce strong NIR extinction over a broad range of wavelengths from 650 to 900 nm, which is of practical interest in biomedical imaging.

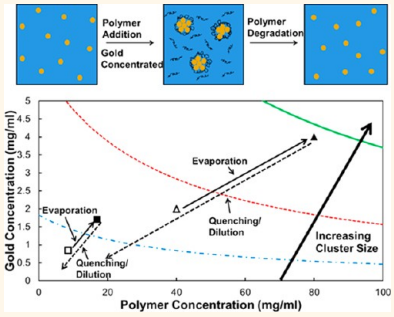

KEYWORDS: nanoclusters · plasmonic nanoparticles · colloidal forces · depletion attraction · biodegradable nanoparticles · equilibrium assembly

Metal nanoclusters composed of primary nanoparticles are of interest in a wide array of applications such as biomedical imaging, catalysis, sensors, and electromagnetic imaging of subsurface reservoirs.[1−6] Structure-directing agents including polymers, dendrimers, proteins, or DNA are often used to template the orientation of the primary particles within the clusters.[7,8] Typically, the amount of inactive templating agents in the product must be 50% or more to direct the assembly. Recently, sub-100 nm nanoclusters of ~5 nm Au primary charged nanoparticles with controlled size were assembled by adding small amounts of stabilizing polymers.[4,5] Additionally, the "self-limiting" assembly of citrate-stabilized cadmium selenide (CdSe) nanoparticles into clusters was observed upon the addition of cadmium perchlorate and sodium selenosulfate precursors in water, as characterized by computer simulation.[6] Furthermore, "kinetically trapped" clusters of controlled size comprising poly(ethylene glycol) (PEG)-stabilized Au nanoparticles have been reported by balancing van der Waals attractive forces with the steric repulsion provided by the PEG layer, which is modulated by the addition of an alkanethiol to the Au nanoparticle surface.[9]

Although aggregates of nanoparticles may be formed by kinetic assembly, the growth often produces large, uncontrolled microparticle aggregates and/or gels upon varying colloidal interactions through pH, salinity,[10] and the addition of polymers to induce depletion attraction.[11] Given the uncertainty in control of the cluster size morphology *via* kinetic assembly, it would be desirable to devise a fundamental strategy to tune cluster architecture and size by equilibrium assembly. If this equilibrium assembly were fully reversible, the clusters may dissociate all the way to monomer upon changes in the solvent conditions.

The equilibrium assembly of nanoparticles into nanoclusters has been reported in

* Address correspondence to kpj@che.utexas.edu.

Received for review August 28, 2012 and accepted December 11, 2012.

Published online December 11, 2012
10.1021/nn303937k

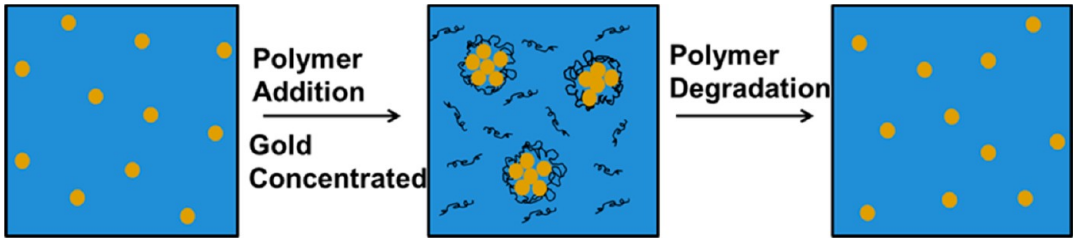

Figure 1. Schematic of quenched equilibrium nanocluster formation and dissociation process. A polymer solution is added to a Au nanoparticle dispersion, and the mixture is then concentrated through partial water evaporation in order to form Au nanoclusters. Polymer degradation upon hydrolysis results in the dissociation of nanoclusters back to primary charged Au nanospheres.

organic solvents[12,13] and more recently in aqueous environments.[6,14] The size of clusters of poly(methylmethacrylate) (PMMA) spheres (~4−10 μm)[12] and Boehmite rods (~350−450 nm)[13] in organic solvents with low dielectric constants is governed by a balance of strong, short-ranged attraction and weak, longer-ranged electrostatic repulsion, as described with a free energy equilibrium model.[15] In aqueous solvents, nanoclusters of primary protein nanocolloids were found to be extremely small[16] and short-lived[17] given strong electrostatic repulsion between primary particles.[15] However, for slightly charged proteins near the isoelectric point, large (~100 nm), long-lived equilibrium clusters of ~10 nm protein molecules were formed.[14] Here, crowder molecules (depletants) were added to balance short-ranged depletion attraction between the protein particles against the long-ranged electrostatic repulsion and thereby tune the cluster size.[14,15] Upon dilution, these clusters reversibly dissociated to stable protein monomers.

To date, it is unknown whether equilibrium nanoclusters may be assembled from inorganic nanoparticles in aqueous media and whether they would reversibly dissociate back to individual nanoparticles. Partially dissociable Au nanoclusters, with sizes <100 nm in diameter, were formed by mixing Au nanoparticle dispersions with small amounts (~20%) of solid polylactic acid (PLA) and PEG copolymer, PLA(1k)-*b*-PEG(10k)-*b*-PLA(1k). The shift in the surface plasmon resonance (SPR) to the near-infrared (NIR) indicated very close spacings between the Au nanoparticles, consistent with the low polymer loadings.[4,5] The cluster formation was attributed to kinetic assembly upon screening the electrostatic repulsion between the primary particles by the weakly adsorbed polymer. Upon biodegradation of the polymer, the clusters underwent significant, but not full, dissociation into ~5.5 nm Au primary particles, according to the measured change in the SPR.

Herein, we demonstrate the assembly of Au nanoclusters with tunable equilibrium sizes from ~20 to ~40 nm, whereby the equilibrium state is quenched by weak adsorption of a triblock copolymer, PLA(1k)-*b*-PEG(10k)-*b*-PLA(1k) stabilizer on the nanocluster surface. Furthermore, the nanoclusters reversibly dissociate completely to ~5 nm Au nanospheres upon biodegradation of the polymeric quencher, as shown in Figure 1. The magnitude of the charge of the mixed ligand monolayer on the Au surfaces was designed to be small enough to enable formation of nanoclusters in the presence of the copolymer, yet sufficiently large for nanocluster dissociation upon dilution after polymer biodegradation. The polymer is shown to induce depletion attraction between the Au spheres to supplement van der Waals attraction to drive assembly of the charged Au nanoparticles into nanoclusters. The equilibrium cluster size is predicted semiquantitatively with a free energy model that balances short-ranged attraction with long-ranged electrostatic repulsion, as a function of the experimentally measured charges on both the primary Au particles and the nanoclusters. Remarkably, the same model describes both Au and protein[14] nanoclusters. The cluster size is tuned with the Au and polymer concentrations in a new process that utilized well-controlled mixing and partial solvent evaporation, as shown in Figure 1. Additionally, polymer adsorption to the Au nanocluster surface quenches the nanoclusters such that their size does not change upon dilution in deionized water. The close spacings of the Au nanoparticles in the clusters produce strong NIR extinction over a broad range in wavelength from 650 to 900 nm. This wavelength range, where blood is weakly absorbing,[18] is of interest in biomedical imaging including photoacoustic imaging,[19−21] photothermal therapy,[22,23] and combined imaging and therapy.[24−26] Furthermore, the nanoclusters are shown to dissociate completely to 5.5 nm Au nanoparticles, which would be small enough for kidney clearance.[27]

RESULTS

Place Exchange of Citrate Ligands with Lysine To Design the Surface Charge. The properties of primary Au nanospheres before and after lysine ligand exchange are given in Table 1. The hydrodynamic diameter (D_H) of nanospheres before ligand exchange was 4.3 ± 0.7 nm (Table 1 and Figure S1a in the Supporting Information), and the extinction at 800 nm, with a Au concentration of 90 μg/mL, was 0.04. As a result, the extinction coefficient at 800 nm (ε_{800}) was 0.44 cm^2/ng. (Table 1 and Figure S1b). The ζ potential was −58.4 ± 5.3 mV (Table 1). The ligand coverage was determined to be

4% w/w by thermogravimetric analysis (TGA) (Table 1), which is similar to the theoretical weight percent of a citrate monolayer on a 4 nm Au nanoparticle (see Supporting Information). The concentration of the citrate-capped Au particle dispersion was determined to be 3.0 ± 0.1 mg Au/mL by flame atomic absorption spectroscopy (FAAS).

After place exchange, the D_H of the lysine/citrate-capped Au nanoparticles was 4.7 ± 0.8 nm (Table 1 and Figure S1a), relatively close to the initial value, indicating that the nanospheres did not aggregate. In addition, the extinction was 0.06 at 800 nm, and the ε_{800} value was similar to that of citrate-capped nanospheres at 0.67 cm^2/ng (Table 1 and Figure S1b). The slight red shift of the peak of the extinction spectra on lysine/citrate nanospheres from 512 to 520 nm (Figure S1b) may be attributed to the change in surface properties and thus local dielectric constants of the nanoparticles upon lysine displacement of citrate.[28] After place exchange, the magnitude of the ζ potential dropped significantly to −16.0 ± 6.6 mV (Table 1), indicating a substantial degree of replacement of negatively charged citrate ligands with positively charged lysine. The ligand weight percentage did not increase from 4% w/w, as may be expected given the similar molecular weights of lysine and citrate of 146 and 192 g/mol, respectively. The XPS spectrum revealed characteristic peaks at ~532 eV for O 1s, ~400 eV for N 1s, ~285 eV for C 1s, and peaks at 88 and 84 eV for Au 4f (Figure S2a). The atomic ratio of nitrogen to oxygen was determined by integration of the O 1s peak (Figure S2b) and the N 1s peak (Figure S2c). Integration of the N 1s peak yielded a peak area of 2387, while integration of the O 1s peak yielded an area of 8574. On the basis of these peak integrations, the nitrogen/oxygen atomic ratio was 0.28. From this value, the lysine/citrate ratio was calculated to be 1.4 (Table 1), as discussed in Supporting Information.

TABLE 1. Properties of Nanospheres before and after Place Exchange

sample	D_H (nm)	ε_{800} (cm^2/ng)	ζ potential (mV)	ligand % by weight (TGA)	lysine/citrate ratio (XPS)
citrate	4.3 ± 0.7	0.44	−58.4 ± 5.3	4	n/a
citrate/lysine	4.7 ± 0.8	0.67	−16.0 ± 6.6	4	1.4

The reduction in nanosphere surface charge after ligand exchange can be correlated to the XPS results of the composition of the mixed surface layer. TGA results on citrate-capped nanospheres (Table 1) indicate that approximately 196 citrate ligands are present per particles (Supporting Information), which corresponds to 196 × 3 = 588 negative charges. Ligand exchange with lysine replaces 3 negative charges with 1 positive charge, such that the 114 lysine ligands and 82 citrate ligands are present after ligand exchange (Supporting Information), which corresponds to an equivalent of (82 × 3) − (114 × 1) = 132 negative charges. Thus, the surface charge magnitude after ligand exchange would be expected to be 132/588 = 22% of the original surface charge, which is in good agreement with the ζ potential values, which dropped to 28% of its original value after lysine ligand exchange. While the actual number of negative charges on the surface cannot be directly captured by ζ potential measurements, the amount of *relative* charge can be compared, as is done here.

Nanocluster Formation by Equilibrium Assembly of the Primary Au Nanoparticles. After ligand exchange, citrate/lysine-capped primary nanoparticles were assembled into nanoclusters, as shown schematically in Figure 1. The morphologies of equilibrium nanoclusters formed *via* the pathways depicted in Figure 1 are shown in Figure 2, based on transmission electron microscopy (TEM), for the Au and polymer concentrations given in Table 2. Images of several 20−4.0 and 20−0.9 particles are shown in Figure S5. These images show densely packed primary Au nanoparticles within each nanocluster. Due to this dense Au packing and the polymer, it can be difficult to discern the boundaries of individual nanospheres. These nanoclusters were purified by centrifugation and redispersed in DI water. Centrifugation removed unclustered primary nanospheres, excess polymer and ligands, and smaller and/or less closely

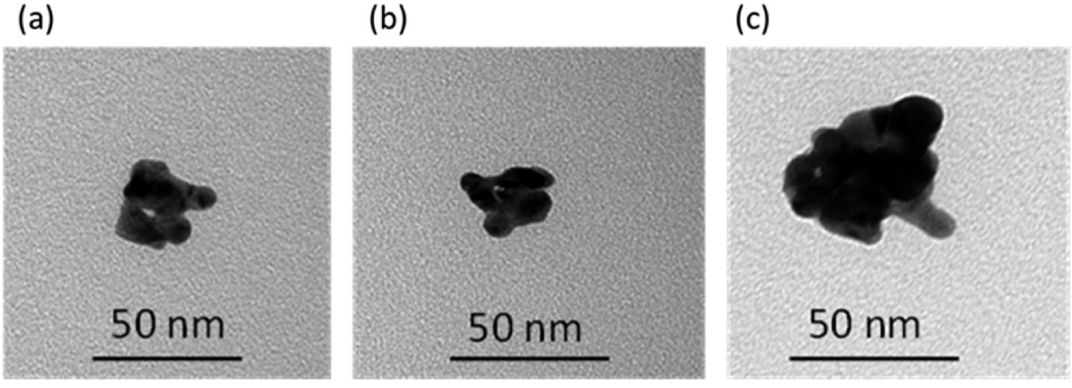

Figure 2. Representative TEM images of nanoclusters formed with a final Au concentration of (a) 0.9 mg/mL (20−0.9), (b) 1.7 mg/mL (20−1.7), and (c) 4.0 mg/mL (20−4.0). All samples had a final polymer/Au ratio of 20/1.

TABLE 2. Properties of Nanoclusters[a]

sample	final Au concn (mg/mL)	final polymer concn (mg/mL)	D_H (nm)	TEM diameter (nm)	ε_{800} (cm^2/ng)	ζ potential (mV)	Au yield by mass (%)
20—0.9	0.9	18	21.4 ± 4.4	24.0 ± 6.2	10.6	−12.3 ± 1.1	17 ± 6
20—1.7	1.7	34	29.4 ± 3.2	31.1 ± 6.9	11.7	−16.4 ± 3.6	31 ± 12
20—4.0	4.0	80	40.1 ± 4.3	42.7 ± 9.4	12.9	−13.2 ± 0.6	61 ± 15
10—1.7	1.7	17	24.0 ± 5.6	21.0 ± 4.3	11.2	−16.7 ± 3.6	26 ± 13
50—1.7	1.7	85	38.4 ± 7.3	36.3 ± 5.6	13.0	−12.5 ± 1.2	57 ± 18

[a] The final Au and polymer concentrations are after solvent evaporation but prior to dilution to harvest the nanoclusters. Sample names contain two numbers separated by a dash: final polymer/Au mass ratio and final Au concentration in mg/mL.

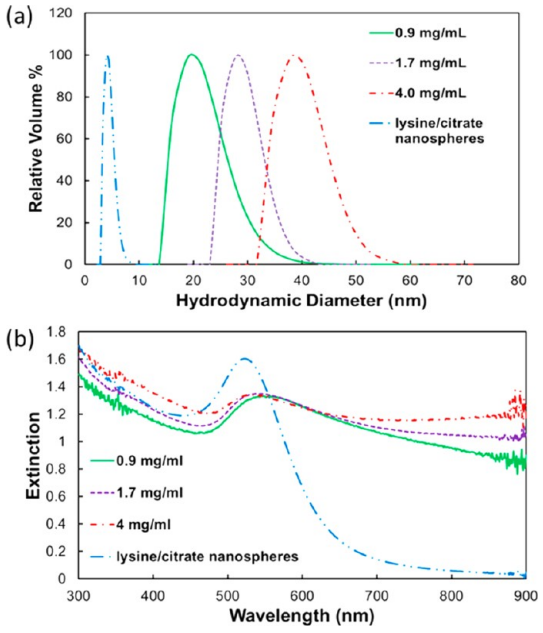

Figure 3. (a) DLS D_H distributions and (b) UV—vis—NIR extinction spectra of nanoclusters formed with 0.9 mg/mL (20—0.9), 1.7 mg/mL (20—1.7), and 4 mg/mL (20—4.0) final Au concentrations. UV—vis—NIR spectra were taken at a Au concentration of ~90 μg/mL. All samples had a polymer/Au ratio of 20/1.

packed nanoclusters, yielding a substantial population of densely packed nanoclusters (as seen by TEM). Nanocluster yields increased with Au concentration and polymer/Au ratio, reaching 61%, as both of these factors will be shown to drive equilibrium nanocluster formation.

The effects of increasing final Au concentration on the Au nanocluster hydrodynamic diameter and optical properties are shown in Figure 3 and Table 2. In the first set of experiments, the polymer/Au ratio was fixed at 20/1. As the final Au concentration is increased from 0.9 to 1.7 mg/mL, the nanocluster D_H increased from 21.4 ± 4.4 to 29.4 ± 3.2 nm (Figure 3a and Table 2). The D_H increased to 40.1 ± 4.3 nm (Figure 3a and Table 2) as the final Au concentration was increased from 1.7 to 4.0 mg/mL. Secondary populations of large aggregates were not observed in either volume-weighted D_H distributions or intensity-weighted D_H distributions, which are more sensitive to large aggregates (Figure S8a). Nanocluster D_H distributions were highly reproducible, as shown for 20—0.9 and 20—4.0 particles in Figure S10.

Furthermore, analysis of TEM images of the nanoclusters (at least 20 clusters in several images analyzed) indicated reasonable agreement between the measured D_H and the nanocluster size measured with TEM (Table 2). For TEM analysis, it is somewhat challenging to discern the boundaries between individual nanoclusters at high surface coverages in the images, relative to simpler geometries such as spheres or rods.[4,5] Thus, we intentionally used low surface coverage on the grids and acquired multiple images of nanoclusters to conduct a sizing analysis. Histograms which present a detailed analysis of the TEM images for 20—0.9, 20—1.7, and 20—4.0 particles are shown in Figure S6. An increase in the final Au concentration from 0.9 to 1.7 mg/mL also increased the extinction at 800 nm from 0.95 to 1.05, thus increasing the extinction coefficient ε_{800} from 10.6 to 11.7 cm^2/ng (Figure 3b and Table 2). Further increase of the final Au concentration from 1.7 to 4.0 mg/mL increased the nanocluster extinction at 800 nm and ε_{800} to 1.16 and 12.9 cm^2/ng (Figure 3b and Table 2), respectively. The nanocluster ζ potential increased in magnitude slightly from −12.3 ± 1.1 mV for 20—0.9 particles to −16.4 ± 3.6 mV for 20—1.7 particles (Table 2). For 20—4.0 particles, the nanocluster ζ potential decreased very slightly in magnitude to −13.2 ± 0.6 mV (Table 2).

For a final Au concentration of 1.7 mg/mL, the morphologies from TEM with increasing polymer/Au concentration for samples 10—1.7, 20—1.7, and 50—1.7 particles are shown in Figure 4. In each case, densely packed Au nanoclusters are observed. The Au yields for 10—1.7, 20—1.7, and 50—1.7 particles were 26 ± 13, 31 ± 12, and 57 ± 18% by mass of Au, respectively, indicating that the increase in polymer concentration facilitated nanocluster formation.

The effects of polymer/Au ratio on nanocluster size and extinction are shown in Figure 5 and Table 2. As the polymer/Au ratio is increased from 10/1 to 20/1, the nanocluster D_H increases modestly from 24.0 ± 5.6 to 29.4 ± 3.2 nm (Figure 5a and Table 2), and increasing the polymer/Au ratio further to 50/1 increased the D_H to 38.4 ± 7.3 nm (Figure 5a and Table 2). Size analysis of TEM images of 10—1.7 and 50—1.7 particles (at least 20 particles in several images analyzed) revealed agreement between D_H distributions measured by dynamic light scattering (DLS) and the size measured by TEM

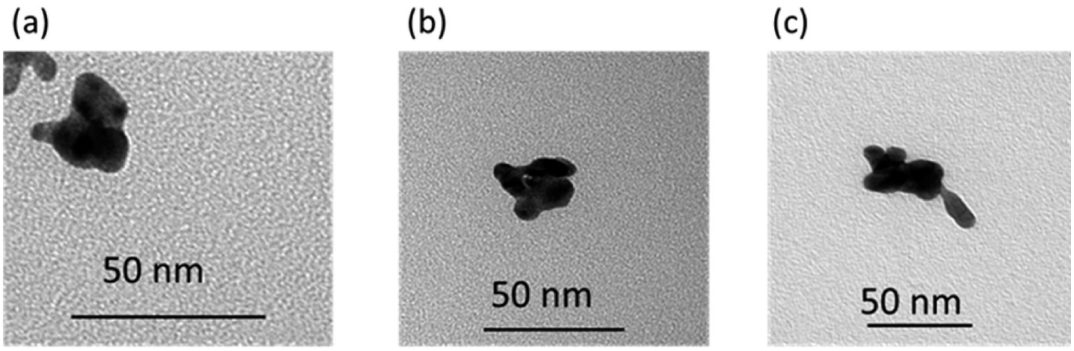

Figure 4. Representative TEM images of nanoclusters formed with a final Au concentration of 1.7 mg/mL and polymer/Au ratio of (a) 10/1 (10−1.7), (b) 20/1 (20−1.7), and (c) 50/1 (50−1.7).

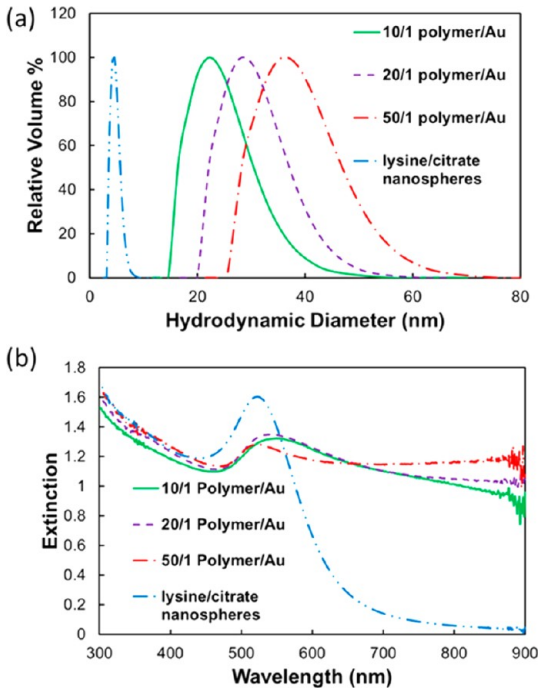

Figure 5. (a) DLS D_H distributions and (b) UV−vis−NIR extinction spectra of nanoclusters formed with polymer/Au ratios of 10/1 (10−1.7), 20/1 (20−1.7), and 50/1 (50−1.7). UV−vis−NIR spectra were taken at a Au concentration of ∼90 μg/mL. All samples had final Au concentrations of 1.7 mg/mL.

analysis (Table 2). TEM histograms for 10−1.7 and 50−1.7 particles are shown in Figure S7. NIR extinction increased with nanocluster D_H, as the extinction at 800 nm increased slightly from 1.01 to 1.05 as polymer/Au ratio was increased from 10/1 to 20/1 (Figure 5b). As a result, the ε_{800} increased from 11.2 to 11.7 cm^2/ng (Figure 5b and Table 2). A further increase in polymer/Au ratio to 50/1 increased the extinction at 800 nm to 1.17 (Figure 5b) and increased ε_{800} to 13.0 cm^2/ng (Figure 5b and Table 2). The nanocluster ζ potential did not change significantly as the polymer/Au ratio was increased from 10/1 to 20/1, while the ζ potential decreased slightly in magnitude to -12.5 ± 1.2 mV for a polymer/Au ratio of 50/1 (Table 2). Large aggregates were not observed in any of these nanocluster samples, even in intensity-weighted D_H distributions (Figure S8). TGA was conducted on 20−0.9, 20−1.7, and 20−4.0 particles. The organic content in the nanoclusters remained fairly constant (Table S1) for 20−0.9 and 20−1.7 particles, but a decrease in organic content from 50 to 31.8% w/w was observed as the nanocluster size increased.

In order to provide further evidence for equilibrium formation of nanoclusters, a control experiment was performed, in which 20−0.9 particles were synthesized with solvent evaporation over approximately 4.5 h, in contrast to only ∼40 min for particles shown in Figures 3 and 4. Here, the extinction spectrum and D_H did not change with evaporation rate (Figure S9), supporting the concept of equilibrium rather than kinetically controlled assembly.

Nanocluster Dissociation. Dissociation of 20−4.0 particles was monitored over 48 h in pH 5 HCl by DLS and UV−vis−NIR spectroscopy. As the incubation time increased from 6 to 48 h, the D_H decreased monotonically from 40.1 ± 4.3 to 5.0 ± 4.3 nm (Figure 6a and Table 3), and the extinction at 800 nm (for a Au concentration of 160 μg/mL) decreased from 1.85 to 1.00. As a result, ε_{800} decreased from 12.9 to 6.3 cm^2/ng (Figure 6b and Table 3). After 48 h in pH 5 HCl, 20−4.0 nanoclusters dissociated nearly completely to monomer. The high standard deviation of the D_H distribution of dissociated nanoclusters indicates very small oligomers are still present, which is supported by the small (∼3% by volume) peak in the size distribution centered around 20 nm as well as the difference between the dissociated nanocluster ε_{800} and the primary particle ε_{800} value of 0.67 cm^2/ng (Table 1). These differences are attributed to dimers, trimers, and undissociated nanoclusters that might still be present in solution and which contribute to the NIR extinction and scattering for DLS.[4] The variation of the natural logarithm of the number of particles per nanocluster *versus* time is shown in Figure 6c. The number of particles in a cluster n_c is determined by eq S6 in Supporting Information. The plot is quite linear with an R^2 value of ∼0.98 (Figure 6c), indicating approximately first-order kinetics. The dissociation of 20−4.0 particles was also highly reproducible for two separate samples, as shown in the kinetics plots in Figure S11. TEM analysis

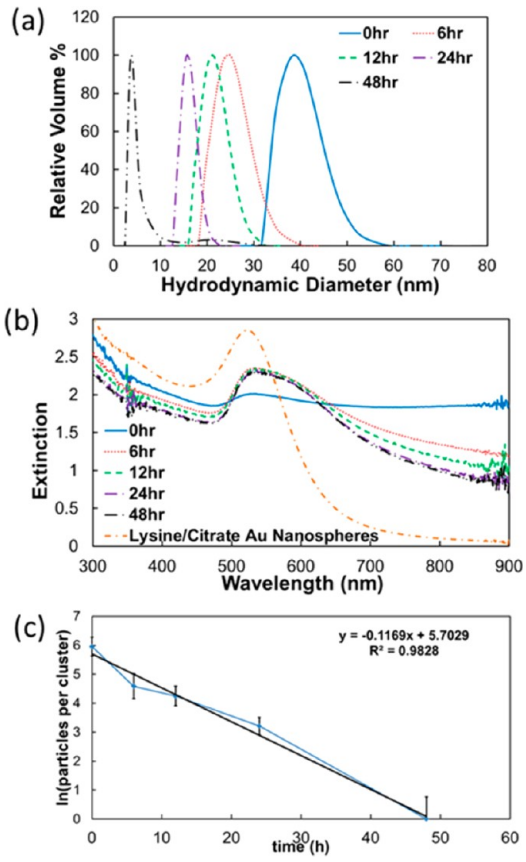

Figure 6. (a) DLS D_H distributions, (b) UV−vis−NIR extinction spectra, and (c) kinetics of dissociation of nanoclusters with a polymer/Au ratio of 20/1 and Au concentration of 4.0 mg/mL (20−4.0 particles) at various times after being exposed to a pH 5 HCl environment. UV−vis−NIR spectra were taken at a Au concentration of ~160 μg/mL. Error bars in (c) correspond to the calculated standard deviation taken from D_H distributions measured by DLS.

TABLE 3. DLS Sizes and Extinction Coefficients of Nanoclusters at Various Dissociation Time Points

incubation time (h)	D_H (nm)	ε_{800} (cm^2/ng)
0	40.1 ± 4.3	12.9
6	25.2 ± 3.6	8.4
12	22.7 ± 2.6	7.4
24	16.1 ± 1.6	6.4
48	5.0 ± 4.3	6.3

of dissociated 20−4.0 particles after 48 h incubation in pH 5 HCl showed similar results as those given by DLS, as the image showed small primary ~5 nm Au nanospheres (Figure S12a).

The nanocluster dissociation was further investigated by also placing 20−1.7 particles into pH 5 HCl. Interestingly, after only 24 h of exposure to HCl, the D_H of 20−1.7 particles decreased all the way from 30.0 ± 3.3 to 4.0 ± 3.1 nm (Figure 7a), and the extinction at 800 nm (for a Au concentration of 60 μg/mL) dropped from 0.71 to 0.06 (Figure 7b). As a result, the ε_{800} dropped from 11.8 to 1.0 cm^2/ng, which is reasonably close to the primary particle ε_{800} value of 0.67 cm^2/ng

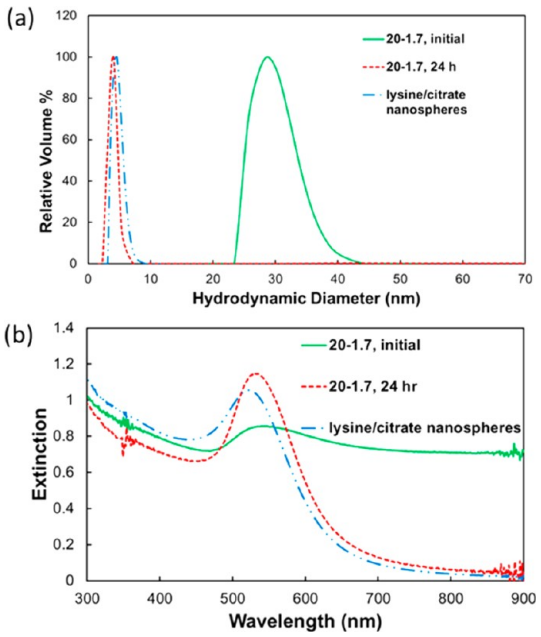

Figure 7. (a) DLS D_H distributions and (b) UV−vis−NIR extinction spectra for nanoclusters with a polymer/Au ratio of 20/1 and a final Au concentration of 1.7 mg/mL (20−1.7 particles) before and after being exposed to a pH 5 HCl environment for 24 h. D_H distributions and UV−vis−NIR spectra of lysine/citrate-capped nanospheres are also included for reference. UV−vis−NIR spectra were taken at a Au concentration of ~60 μg/mL.

(Table 1). Here, only 0.4% of the particles by volume show a D_H above 5.5 nm, thus leading to the lower standard deviation in the DLS distribution as well as the lower ε_{800} relative to dissociated 20−4.0 particles. TEM analysis of dissociated 20−1.7 particles after 24 h in pH 5 HCl showed ~5 nm primary Au nanospheres, as shown in Figure S12b.

DISCUSSION

Equilibrium Cluster Size Model. The equilibrium formation of nanoclusters of primary nanoparticles may be shown to be governed by a balance of short-ranged attractive forces with longer-ranged electrostatic repulsion[29,30] as described with a free energy model.[12,14−16,31] An equilibrium nanocluster with a diameter D_c is depicted in Figure 8, along with primary nanoparticles with charge of magnitude q. A fraction of the counterions within the nanocluster dissociate and leave the cluster. As the total nanocluster charge grows with added monomer, eventually, the cluster reaches an equilibrium size when the electric field from the nanocluster repels addition of further monomer. Here, short-ranged attractive forces between individual nanoparticle monomers which favor cluster growth are mediated by longer-ranged electrostatic repulsion at the monomer-cluster levels.

The free energy model describes the assembly of n_c primary particles into a cluster of radius R_c.[14,15] Here, the magnitude of attractive interaction between two

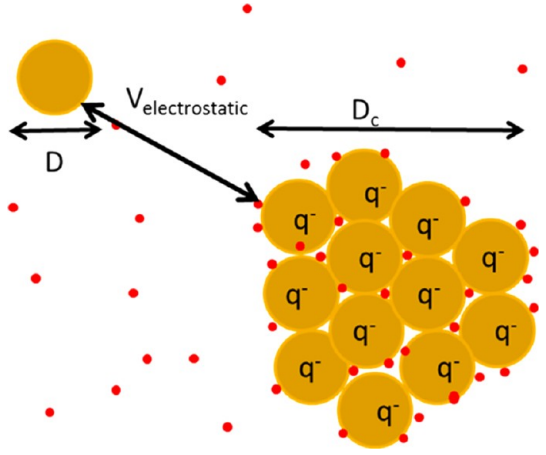

Figure 8. Equilibrium nanocluster with diameter D_c composed of primary particles (of diameter D) each with ion pairs and a negative charge of magnitude q. The highly charged monomer coated with ligands (negligible ion pairing) on the top left is repelled by the charged nanocluster ($V_{electrostatic}$). Bound and free counterions are represented by red dots.

primary particles with C nearest neighbors is represented by a. The surface energy of the cluster is $4\pi R_c^2\gamma$, where the surface tension γ is approximated as $a/4\pi R^2$, where R is the radius of the primary particle. The attractive component of the free energy is then

$$F_A = -\frac{aCn_c}{2} + a\left(\frac{R_c}{R}\right)^2 \quad (1)$$

The repulsive component to cluster free energy is approximated by the expression for a uniform distribution of point charges within a sphere

$$F_R = \frac{3\lambda_b k_B T n_c^2 q^2}{5R_c} \quad (2)$$

where λ_b is the Bjerrum length

$$\lambda_b = \frac{e^2}{4\pi\varepsilon_r\varepsilon_0 k_B T} \quad (3)$$

Here, e is the elementary unit of charge, ε_r is the dielectric constant within the nanocluster, and ε_0 is the relative permittivity of free space.

The minimization of the free energy with respect to the cluster radius R_c yields the following expression for equilibrium cluster size:

$$n^* = \frac{5aR}{6\lambda_b k_B T q^2} \quad (4)$$

where n^* is the equilibrium number of monomers per cluster. From eq 4, the cluster size increases with the magnitude of attraction a between primary particles and decreases with the magnitude of charge q. More recently, this theory was extended to include the effect of the fractal dimension of the cluster and was shown to capture the trends in the size of protein nanoclusters, by fitting ε_r and the number of dissociable ion sites per primary particle, σs (Supporting Information), as adjustable parameters.[14]

The experimentally observed correlation between polymer concentration and nanocluster size led us to postulate that polymer-induced depletion attraction plays an important role in nanocluster formation. Upon addition of the weakly adsorbing triblock copolymer, an osmotic pressure gradient is produced from the exclusion of the polymer from the gap between Au particles. This pressure gradient creates an attractive force ("depletion attraction") between the Au nanoparticles. Depletion interactions, which have been carefully characterized in other related systems (see, *e.g.*, Edwards and Bevan,[32] Piech and Walz,[33] and Kulkarni *et al.*[34]), are strongly dependent on polymer concentration and the distance between Au particles.[35] We estimate the depletion potential using the Asakura–Oosawa potential,[36,37] which can be written as[35]

$$\frac{V_{dep}}{kT} = -\left(\frac{R_g}{R}\right)^{-3}\left(\frac{c_p}{c^*}\right)\left(\frac{R_g}{R} - \frac{H}{2R}\right)^2\left(\frac{3}{2} + \frac{R_g}{R} + \frac{H}{4R}\right) \quad (5)$$

where R_g is the radius of gyration of the polymer depletant, c_p is the polymer concentration, and c^* is the overlap concentration where polymer chains begin to overlap, which is defined as[35]

$$c^* = \frac{3M}{4\pi R_g^3 N_{av}} \quad (6)$$

where M is the molecular weight of the polymer and N_{av} is Avogadro's number. Here, we assume that the polymer micelles may be approximated by a PEG chain with a hydrodynamic radius (R_h) equivalent to the radius of the micelle, which was measured to be 7 nm.[5] This assumption is reasonable since the triblock copolymer is mostly composed of PEG. The calculation of the molecular weight of the micelle from the hydrodynamic diameter is given in Supporting Information.

Equilibrium Assembly of Au Nanoclusters. The assembly of ~5 nm Au nanoparticles into nanoclusters will now be described in terms of the colloidal forces shown schematically in Figure 8. The magnitude of the charge on primary particles was initially reduced by replacing some of the citrate ligands (charge of −3) with cationic lysine ligands (charge of +1) to create a mixed charge monolayer.[38] The resulting reduction in the ζ potential magnitude from −58 to −16 mV will be shown to favor nanocluster formation below.

Equilibrium nanocluster diameters (D_c) predicted by the free energy model are shown to increase over a selected range of 20−40 nm with increasing c_{Au} and/or c_p in Figure 9.[14,15] The theoretical model, despite its simplicity, semiquantitatively predicts the experimental data. The parameters in the model, shown in Table S2, are discussed in detail in the Supporting Information. The total number of charges on the primary nanoparticles in water, 2.78, was determined from ζ potential measurements on lysine/citrate-capped primary particles (Table 1)

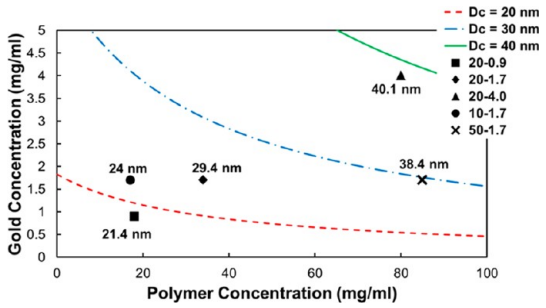

Figure 9. Cluster size contours for various values of polymer and Au concentration, based on the equilibrium free energy model discussed in the text. Hydrodynamic diameters (DLS) shown by points are in reasonable agreement with the model.

using eq S6. The charge on a Au nanoparticle within the nanoclusters q was determined by calculating the total number of charges per nanocluster from the measured ζ potentials using eq S6, as shown in Supporting Information, and the number of nanoparticles in a cluster from eq S7. We chose a local dielectric constant in the dense nanoclusters of 25, approximately capturing the expected loss with respect to bulk water, as described further in Supporting Information. This value is the only adjustable parameter in the model. The interparticle distance in the model was assumed to be 1 nm, which is reasonable because of the high NIR extinction and dense morphologies observed within the nanoclusters. Additionally, the equilibrium model is not very sensitive to interparticle distance, as further discussed in Supporting Information.

The rate of depletion-attraction-induced cluster assembly is assumed to be much faster than the rate of polymer adsorption on Au. This is a reasonable assumption given the very low affinity of the dominant PEG block for Au. While depletion attraction is the first effect of the polymer during nanocluster formation, the slower polymer adsorption quenches the final nanocluster size. Thus, we treat the nanocluster formation process, prior to polymer adsorption, as a pseudo-equilibrium process.

As the polymer concentration c_p increases, depletion attraction raises the overall attraction a in eq 4, consequently increasing the nanocluster size. This trend is shown in Table 2 and Figure 9 for a final Au concentration of 1.7 mg/mL. Note that the theory mildly underpredicts D_H for the highest polymer concentration (50−1.7). As the number of monomers in the cluster increases, the charge per cluster determined from the ζ potential increases. This experimental charge in the nanocluster, relative to the total charge expected based on the initial charge on each primary particle, was only 11.0% for the 10−1.7 cluster, indicating significant ion pairing. Furthermore, this ratio decreased monotonically from 11.0 to 4.3% (Table 4) as the cluster size increased with c_p. Additionally, an increase in final c_{Au} leads to a decrease in the charge per particle q since fewer counterions are required to dissociate per volume to provide the same entropic gain, as shown in eq S11. As the charge decreases, the equilibrium nanocluster size increases, according to eq 4. Thus, as the final c_{Au} is increased, D_c increases.

TABLE 4. ζ Potentials and Charges Per Cluster (Experimental, Based on ζ Potential and Aggregation Number) Compared with Calculated Charge if All Monomers Stayed Fully Charged upon Cluster Formation

sample	ζ potential (mV)	negative charges per cluster	negative charges per cluster calcd	% charge retained
20−0.9	−12.3 ± 1.1	15.1	157	10.0
20−1.7	−16.4 ± 3.6	33.0	407	8.1
20−4.0	−13.2 ± 0.6	44.2	1033	4.3
10−1.7	−16.7 ± 3.6	24.4	221	11.0
50−1.7	−12.5 ± 1.2	38.8	907	4.3

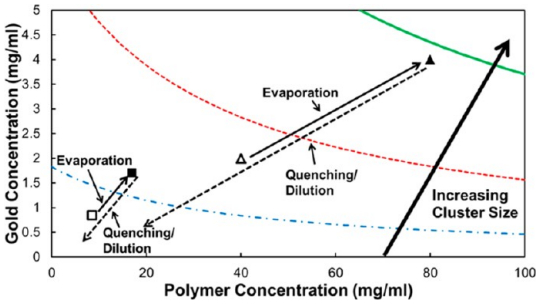

Figure 10. Schematic of equilibrium nanocluster formation process followed by polymer quenching. Curves of constant cluster diameter (D_c) as a function of polymer and Au concentrations are shown as countours predicted from the equilibrium free energy model discussed in the text and parameters in Table S2. Open symbols represent concentrations upon mixing of polymer and Au nanoparticle solutions, and filled symbols represent Au and polymer concentrations after evaporation of 50% of the solvent. Solid lines represent the evaporation process, and dashed lines represent the dilution of the quenched clusters, during which nanocluster size is constant (*i.e.*, quenched due to polymer adsorption). Process lines are presented for 20−4.0 (triangles) and 10−1.7 particles (squares).

The combined effect of increased depletion attraction and reduction in charge is seen experimentally through the variance in final Au concentration while maintaining a constant polymer/Au ratio. As c_{Au} is increased from 0.9 mg/mL (20−0.9 particles) to 4.0 mg/mL (20−4.0 particles), the enhanced depletion attraction as well as the reduced Coulombic repulsion increases the D_c of the cluster. The decrease in q is shown in Table 4, as the charge retained in a nanocluster decreases monotonically from 10.0 to 4.3% (Table 4), due to entropic effects. Thus, the experimental nanocluster sizes are predicted semi-quantitatively by the theoretical model.

Nanocluster formation pathways are illustrated schematically in Figure 10. Here, open symbols represent the Au and polymer concentrations resulting from the mixing of polymer and Au nanoparticle solutions. Evaporation of water from these mixed solutions is shown by the solid lines with arrows, resulting in the final Au and c_p represented by the solid symbols

(Figure 10). During solvent evaporation, the increase in c_p increases the magnitude of polymer-induced depletion attraction between particles, as is shown by eq 5. In addition, the increase in c_{Au} decreases the charge, as shown in eq S11. Both of these factors increase the cluster size.

Quenching of Nanocluster Size. After assembly of the Au nanospheres into nanoclusters, this quasi-equilibrium state is quenched by irreversible polymer adsorption. The hydrophobic nature of the PLA groups in the PLA-PEG-PLA triblock copolymer drives the polymer adsorption on the hydrophobic Au surface.[39] The rate of this polymer adsorption, however, is expected to be much slower than the rate of depletion-attraction-induced equilibrium particle assembly. The weak driving force for adsorption reflects the large amount of hydrophilic PEG in the polymer which interacts only weakly with the hydrophobic Au surface.[39] If polymer adsorbed on individual Au spheres, which then formed clusters, the Au primary particle spacings would be too large for the intense NIR extinction observed in Figures 3b and 5b. Instead, the slow kinetics of polymer adsorption relative to rapid nanocluster formation led to very closely spaced Au particles. Additionally, the adsorbed polymer provided steric stabilization on the nanoclusters' surface. To harvest the nanoclusters, they were rapidly diluted in deionized water, as shown by the dashed lines in Figure 10. Here, the cluster size did not change. The high degree of dilution would lead to Au monomer particles according the equilibrium model (Figure 10). Instead, the irreversible polymer adsorption on the nanocluster surface maintained a "quenched" equilibrium cluster size. Furthermore, attraction between the highly ion paired Au primary particles within the cluster with low charge prevented nanocluster dissociation. The polymer played a multifunctional role in (1) driving the depletion attraction to assemble the primary Au particles into clusters, (2) providing steric stabilization of the clusters, and (3) quenching the nanoclusters with an equilibrium size. The clusters were fairly dilute and colloidally stable over weeks, so we did not calculate the interaction potential between the clusters.

The concept of quenched equilibrium Au nanoclusters presented in this work is substantially different from our previous Au nanocluster studies, which attributed nanocluster formation to a kinetic assembly mechanism.[5] In our previous work, a kinetic stability ratio was estimated based on the time required for a qualitative color change in the nanocluster dispersion by eye during formation.[5] This approach was not applicable to nanoclusters smaller than 50 nm, where the color change was very rapid and heavily dependent upon the evaporation rate of the solvent. The previous work did not recognize the depletion force was sufficiently strong to produce equilibrium assembly (given the micelle concentration was unknown), and thus equilibrium assembly was not thought to be present.[5] Furthermore, the composition of the ligands on the surface was not measured, and the charge on the Au surface was not well-characterized, which limited the analysis of the formation mechanism.[4,5] In most cases, all of the water was evaporated to form Au-polymer films which were later diluted to harvest the clusters. This two-step approach may involve complex cluster formation mechanisms. As a result, the present study represents a major and novel advance over previous work by demonstrating equilibrium nanocluster assembly and control over nanocluster size.

In an insightful related study, "self-limiting" clusters of CdSe primary particles have been observed in water, where cluster growth stopped upon reaching a balance between charge in the cluster and van der Waals attraction between particles.[6] Both nanocluster size and ζ potential measurements showed cluster growth followed by a plateau as the self-limited cluster state was reached.[6] Building upon this self-limiting nanocluster concept, a novel aspect of the present work is that degradation of the polymer quencher allows for reversible cluster dissociation to recover ~5 nm monomers, which is critical for effective renal clearance. Moreover, the present study demonstrates the ability to tune nanocluster size by balancing effective colloidal interactions as well as the ability to semiquantitatively predict this cluster size.

In the current study, we chose to form nanoclusters at a desired evaporation extent of only 50% and from primary Au nanospheres with a ζ potential of only −16 mV. If the ζ potential of the primary nanospheres were more negative, electrostatic repulsion would be too dominant, and the size would be too small, as shown in eq 4. For example, for highly charged Au particles with only citrate ligands, the required evaporation extent was 85% to form nanoclusters, as would be evident in Figure 10. However, at such high evaporation amounts, the particles form a viscous gel and it may become difficult to redisperse the clusters with the desired size and with low polydispersity.

For particular experimental pathways, other than those in Table 1 and Figure 10, we observed kinetic traps that prevented attainment of the sizes predicted by the equilibrium model. For example, adding polymer solution in one step, instead of iteratively, to the Au solution led to large nanoclusters with weak NIR extinction. Immediately after mixing the Au dispersion with the polymer solution, we observed a large increase in viscosity, which may have limited access to equilibrium configurations, leading to relatively large ~120 nm aggregates with weak NIR extinction (Figure S4). In addition, initial Au concentrations in excess of 6 mg/mL led to irreversible aggregation of nanoparticles even without adding any polymer, indicating insufficient electrostatic stabilization.

These quenched equilibrium Au nanoclusters are quite different from other clusters which are affected

by dilution, such as protein nanoclusters[14] as well as clusters of cerium oxide[40] and iron oxide[41] nanoparticles and oppositely charged diblock polymers. The size of kinetically "frozen" clusters of cerium oxide, from 100 to 500 nm in diameter, has been shown to change with dilution rate, with smaller clusters formed at faster dilution rates.[40] Equilibrium Au nanoclusters, if quenched by irreversible polymer adsorption, in contrast, do not change size after dilution.

Nanocluster Dissociation. For a Au dispersion without polymer present, depletion attraction between Au nanoparticles is not present and the equilibrium state was found to be individual charged primary particles (Figure 10). For polymer-coated Au nanoclusters, dissociation was initiated by exposure to a pH 5 HCl environment, which accelerates the degradation rate of the PLA segments, relative to pH 7.[42] As the polymeric quencher was gradually removed upon hydrolysis, the cluster size decreased continuously as charged Au primary particles left the nanocluster surface. After 48 h, enough polymer had degraded for the 20−4.0 nanoclusters to dissociate almost completely to monomer.

The plot of $\ln(n_c)$ *versus* time shown in Figure 6c indicates approximately first-order kinetics, as demonstrated in eq 6:

$$\frac{dn_c}{dt} = -kn_c \qquad (6)$$

Here, n_c is the number of particles in a cluster, given by eq S7, and k is the first-order rate constant. The linear fit to the data shown in Figure 6c reveals a k of ~0.12 h^{-1}.

The dissociation of the smaller 20−1.7 nanoclusters was faster and more complete (Figure 7) relative to the larger 20−4.0 ones. For the smaller nanocluter size, less time is needed to degrade the smaller amount of polymeric quencher, for a fixed polymer/Au ratio. Additionally, there are fewer chances for dissociating nanoclusters to become trapped in metastable irreversible states involving even a small number dimers, trimers, and higher-order assemblies. The NIR extinction is significant for dimers and trimers at close spacing,[5] as seen in Figure 6 with 20−4.0 particles. The complete dissociation to charged Au monomer nanospheres supports the quenched equilibrium concept, whereby the polymer no longer influences the Au particle size after it is degraded. After PLA hydrolysis, the PEG central block did not have a tendency to adsorb strongly on Au,[39] and during dissociation, the polymer concentration was too low to produce depletion attraction.

Nanocluster Spectral Properties. The surface plasmon resonance for Au nanoparticles is well-known to shift to the NIR for various morphologies including nanoshells,[23,24,43,44] nanocages,[45,46] high aspect ratio nanorods,[47,48] nanoflowers,[49,50] or nanostars.[51,52] These particles with NIR extinction, however, often have diameters greater than 5.5 nm in diameter, which would be too large for efficient kidney clearance from the body.[27] Alternatively, the SPR has been experimentally demonstrated to shift toward the NIR for dimers and trimers of Au nanospheres,[43] and broad NIR extinction has been observed in larger clusters of Au nanospheres.[4,5] The amount of extinction broadening has been shown to be dependent on the interparticle spacing between constituent particles.[43] In the present work, intense NIR extinction is achieved *via* extremely close (less than a particle diameter[8,53]) interparticle spacings within Au nanoclusters. As the polymer/Au ratio is increased, the corresponding increase in depletion attraction can potentially decrease the interparticle spacing, while simultaneously increasing nanocluster size. As a result, the amount of NIR extinction increases, as is shown in Figure 5b. In addition, as the final Au concentration was increased (along with the final polymer concentration), the charge per primary particle in a cluster was decreased, potentially decreasing the interparticle spacing and increasing nanocluster size. The resultant increase in cluster size and decrease in interparticle spacings creates broader extinction spectra and greater NIR extinction (Figure 3b).

The Au nanoclusters exhibited intense NIR extinction which is of interest in applications such as photoacoustic imaging[20] and photothermal therapy.[22,23,44] The fine control over nanocluster size demonstrated in this study from ~20 to ~40 nm is in an optimal range for cell uptake[54] and blood circulation.[55] In addition, the biodegradability of these nanoclusters into ~5 nm primary particles offers the possibility of clearance *via* the kidneys.[27] In future applications, the nanoclusters would potentially be targeted to cancer cells *via* biomarkers such as epidermal growth factor receptor (EGFR) and consequently undergo endosomal uptake.[56] Multiple studies have demonstrated that after intravascular (IV) administration in tumor animal models, injected nanoparticles accumulate mostly in the liver, spleen, and tumor.[57] Since nanoclusters have been shown to dissociate within acidic endosomal and lysosomal compartments,[4] we hypothesize that the nanoclusters in this work will dissociate completely to primary particles in the acidic endosomal/lysosomal cellular compartments, and that these particles will then be cleared from the body.

CONCLUSIONS

Equilibrium phenomena play a major role in governing the size of Au nanoclusters, which are quenched by irreversibly adsorbed polymer on the surface. Upon biodegradation of various amounts of the quencher, PLA(1k)-*b*-PEG(10k)-*b*-PLA(1k), the clusters reversibly become smaller and eventually dissociate completely to ~5 nm Au monomer nanospheres. Nanocluster size was tuned from ~20 to ~40 nm by varying the ratio of polymer/Au from 10/1 to 50/1 w/w, to vary the depletion attraction induced by the polymer, and also by varying the Au nanoparticle concentrations from 0.9 to

4 mg/mL. The surface charge on primary Au nanospheres was modified by the addition of positively charged lysine to originally citrate-capped nanospheres to create a mixed charge monolayer on the Au nanosphere surface. The incremental mixing of the polymer solution with the initial Au dispersion, along with solvent evaporation to raise Au and polymer concentrations, provided exquisite regulation of the nanocluster size. The size was predicted semiquantitatively with an equilibrium free energy model as a function of the Au concentration and the polymer/Au ratio. The free energy model describes the balance between long-ranged electrostatic repulsion between primary Au nanospheres with short-ranged van der Waals and depletion attractive interactions. The equilibrium size is quenched by an irreversibly adsorbed polymer layer on the nanocluster surface and remains constant even after removal of excess polymer. The close spacings of primary nanospheres within the nanoclusters resulted in high NIR extinction for all sizes of nanoclusters explored in this work. Thus, a general concept has been demonstrated for forming quenched equilibrium nanoclusters with tunable sizes (and in this case NIR extinction), which reversibly dissociate upon biodegradation of the polymer quencher.

METHODS

Materials. $HAuCl_4 \cdot 3H_2O$ was obtained from MP Biomedicals LLC (Solon, OH), and $Na_3C_3H_5O(COO)_3 \cdot 2H_2O$ was acquired from Fisher Scientific (Fair Lawn, NJ). $NaBH_4$ was also obtained from Fisher Scientific. L-(+)-Lysine was purchased from Acros Chemicals (Morris Plains, NJ), and PLA(1k)-*b*-PEG(10k)-*b*-PLA(1k) was obtained from Sigma-Aldrich (St. Louis, MO).

Synthesis of Citrate-Capped Au Nanospheres and Lysine Ligand Exchange. Citrate-capped Au nanospheres (~4 nm) were formed by reduction of $HAuCl_4$ with $NaBH_4$ by scaling up an earlier method and purifying synthesized particles with tangential flow filtration, as described in Supporting Information.[5] The synthesis resulted in ~25 mL of 3 mg/mL Au.

Lysine place exchange was conducted by adding 20 μL of freshly prepared aqueous solution of 5% w/v (50 mg/mL) lysine to 1.2 mL of the 3 mg/mL citrate-capped Au nanosphere dispersion. Here the pH of the solution increased from pH ~6 to pH ~8.8 upon addition of the basic lysine ligand. At pH 8.8, lysine has two positive charges and one negative charge.[58] After lysine addition, the mixture was stirred for 15 min at room temperature to enable place exchange. Immediately after this reaction, nanosphere samples were either ultracentrifuged for X-ray photoelectron spectroscopy (XPS) or thermogravimetric analysis (TGA), diluted for dynamic light scattering (DLS), UV−visible−NIR (UV−vis−NIR) spectroscopy, or ζ potential analysis, or used to form nanoclusters.

Nanocluster Formation. Immediately after 15 min of lysine place exchange, Au nanospheres were used to form nanoclusters. An aqueous, 120 mg/mL solution of PLA(1k)-*b*-PEG(10k)-*b*-PLA(1k) was freshly prepared. In the base case, the lysine/citrate-capped Au dispersion was diluted to 1 mg/mL from 3 mg/mL. Then, 500 μL of the PLA(1k)-*b*-PEG(10k)-*b*-PLA(1k) solution was then added to 3 mL of 1 mg/mL lysine/citrate-capped Au nanospheres in five iterations of 100 μL each over 10 min. The addition of polymer solution was done under vigorous stirring. After addition of the polymer solution, the resulting Au concentration was 0.9 mg/mL, and the polymer concentration was 17 mg/mL. This mixture was placed in a 19 × 48 mm glass vial, and the vial was placed in a 40 °C water bath and stirred using a magnetic stirrer. Dried air was blown gently over the sample *via* a small tube that was inserted a few centimeters into the vial. The combination of water bath and airflow kept the sample temperature at 25 ± 3 °C as the sample was evaporated to 50% of its original volume over ~40 min, resulting in final Au and polymer concentrations of 1.7 and 36 mg/mL, respectively. These base case samples were denoted 20−1.7 particles, designating to a polymer/Au ratio of 20/1 and a final Au concentration of 1.7 mg/mL (nomenclature adopted throughout). After sample evaporation, the cluster formation was terminated by adding 30 mL of DI water to dilute the Au. The solution was then centrifuged at 10 000 rpm for 10 min in order to separate unclustered and loosely bound particles from the ~30% (by mass) dense Au nanoclusters.

The nanocluster formation process described above was carried out at initial Au concentrations (after addition of polymer solution) from 0.5 to 2.0 mg/mL, and initial polymer concentrations of 9, 40, 8.5, and 42.5 mg/mL (after polymer solution addition). Evaporation, centrifugation, and redispersion were carried out in a manner identical to 20−1.7 particles.

Characterization of Primary Au Nanospheres. After lysine place exchange, samples were diluted to ~0.04 mg/mL in DI water for DLS measurements, measurement of ζ potential, and UV−vis−NIR spectroscopy measurements, without purification. DLS measurements were taken using a custom-built apparatus at a scattering angle of 45° using an avalanche photodiode at ~25 °C.[59] Data were analyzed using a digital autocorrelator (Brookhaven BI-9000AT) and the CONTIN method. The Stokes−Einstein equation was used to obtain a volume-weighted distribution of hydrodynamic diameters (D_H). UV−vis−NIR spectroscopy was performed using a Varian Cary 3E spectrophotometer with a 1 cm path length. UV−vis−NIR extinction measurements were all conducted at a Au concentration of ~90 μg/mL. Extinction values at 800 nm were used to calculate extinction coefficients (ε_{800}) for nanospheres, as described in Supporting Information. The ζ analysis was conducted using a Brookhaven ZetaPlus ζ potential analyzer. Samples were diluted to ~0.02−0.04 mg/mL in 1 mM KCl at pH 7, and the average and standard deviations for 30 single-cycle measurements are reported. Due to the small size of the nanospheres (see Results), the Huckel model was used to relate the measured electrophoretic mobility to a ζ potential.[60]

For TGA and XPS analysis, nanosphere samples were ultracentrifuged for 45 min at 40 000 rpm in order to remove excess citrate and lysine ligands, and the resulting pellet was dried. TGA was performed using a Mettler Toledo TGA/DSC 1 STAR^e system with a gas controller (GC 200) and a temperature set at 22 °C (Julabo). TGA samples were initially heated to 100 °C and held at that temperature for 10 min to eliminate any residual moisture remaining in the samples. The samples were subsequently heated to 900 °C at a heating rate of 20 °C/min, and the mass loss of organic content of the samples was determined.

XPS analysis was performed using a Kratos AXIS Ultra DLD spectrometer equipped with a monochromatic Al X-ray source (Al α, 1.4866 keV). High-resolution elemental analysis was performed on the Au 4f, C 1s, N 1s, and O 1s regions with pass energies of 30, 20, 40, and 20 eV, respectively. A 0.1 eV step and a 4 s dwell time was used in all cases. Charge compensation was not used because of the conductivity of each sample. Peak positions and areas were calculated using a Gaussian + Lorentzian fit and a Shirley background correction.

Au concentrations in nanosphere samples were determined using flame atomic absorption spectroscopy (FAAS) using a GBC FAAS analyzer (GBC Scientific Equipment Pty Ltd., GBC 908AA) with an air-acetylene flame and at a wavelength of 242.8 nm. Samples were diluted, without purification, in aqua regia to between 1 and 5 ppm before analysis.

Nanocluster Characterization. Nanocluster morphologies were observed by transmission electron microscopy (TEM) performed

on an FEI TECNAI G2 F20 X-TWIN TEM using a high-angle annular dark-field detector. Samples were prepared by dipping 200 mesh copper-coated carbon TEM grids (Electron Microscopy Sciences, Hatfield, PA) into liquid nitrogen and then pipetting 5 μL of a dilute nanocluster dispersion onto the grid. The grid was then dried using a VirTis AdVantage tray lyophilizer (VirTis, Gardiner, NY). Unless otherwise noted, DLS, UV−vis−NIR spectroscopy, ζ analysis, and FAAS were performed identically to nanosphere characterization. DLS was conducted on a Brookhaven ZetaPALS analyzer with a scattering angle of 90°. Due to nanocluster size (see Results), the Huckel model was also used to fit measured electrophoretic mobilities in ζ analysis.[60] TGA was conducted on nanoclusters after centrifugation without the ultracentrifugation necessary for nanospheres, using a Mettler-Toledo TGA/SDTA851e instrument.

Nanocluster Dissociation. Dissociation of 20−4.0 and 20−1.7 particles was performed *via* dilution in pH 5 HCl. Dissociation of 20−4.0 particles was monitored by adding ∼200 μL of ∼1.6 mg/mL nanocluster dispersion to 2 mL of pH 5 HCl, such that the Au concentration was ∼160 μg/mL. For 20−1.7 particles, ∼200 μL of a ∼0.4 mg/mL nanocluster dispersion was added to 2 mL of pH 5 HCl, such that the Au concentration was ∼60 μg/mL. Addition of the pH 7 nanocluster dispersion did not change the mixture pH from pH 5 in either case. Nanoclusters were analyzed *via* UV−vis−NIR spectroscopy and DLS without further dilution at 6, 12, 24, and 48 h time points for 20−4.0 particles and after 24 h for 20−1.7 particles. DLS was performed at a scattering angle of 45°, similar to the case for nanospheres.

Conflict of Interest: The authors declare no competing financial interest.

Acknowledgment. K.P.J. and K.S. acknowledge support from NSF Grant CBET-0968038 and the National Institutes of Health Grant CA143663. T.M.T. acknowledges support of the Welch Foundation (F-1696) and the National Science Foundation (CBET-1065357). K.P.J. acknowledges support from the Welch Foundation (F-1319). We acknowledge helpful discussions with S. Jiang on mixed monolayers, and D. Weitz for the role of local dielectric constant in clusters. We thank W. Hardin for XPS, and B. Nielson and C. Bielawski for TGA of nanoclusters.

Supporting Information Available: Synthesis of citrate-capped Au nanospheres, theoretical ligand monolayer calculations, extinction coefficient calculation, XPS ligand ratio determination, theoretical charge screening calculation, equilibrium model details, reduced dielectric constant in clusters, DLS distributions and UV−vis−NIR spectra for primary particles, XPS spectra for primary particles, theoretical depletion interaction potentials, DLS size distribution and UV−vis−NIR spectra for nonclosely spaced clusters, zoomed-out TEM images of 20−4.0 and 20−0.9 particles, intensity-weighted DLS distributions of nanoclusters, DLS size distributions and UV−vis−NIR spectra for 20−0.9 particles made at fast and slow evaporation rates, reproducibility of DLS distributions of 20−4.0 and 20−0.9 particles, reproducibility of dissociation kinetics of 20−4.0 particles, TEM images of dissociated 20−4.0 and 20−1.7 particles, table of parameters for equilibrium model, TGA results for nanoclusters, and histograms of TEM size analysis. This material is available free of charge *via* the Internet at http://pubs.acs.org.

REFERENCES AND NOTES

1. Boal, A. K.; Ilhan, F.; DeRouchey, J. E.; Thurn-Albrecht, T.; Russell, T. P.; Rotello, V. M. Self-Assembly of Nanoparticles into Structured Spherical and Network Aggregates. *Nature* **2000**, *404*, 746–748.
2. Shenhar, R.; Norsten, T. B.; Rotello, V. M. Polymer-Mediated Nanoparticle Assembly: Structural Control and Applications. *Adv. Mater.* **2005**, *17*, 657–669.
3. Ma, L. L.; Feldman, M. D.; Tam, J. M.; Paranjape, A. S.; Cheruki, K. K.; Larson, T. A.; Tam, J. O.; Ingram, D. R.; Paramita, V.; Villard, J. W.; *et al.* Small Multifunctional Nanoclusters (Nanoroses) for Targeted Cellular Imaging and Therapy. *ACS Nano* **2009**, *3*, 2686–2696.
4. Tam, J. M.; Tam, J. O.; Murthy, A.; Ingram, D. R.; Ma, L. L.; Travis, K.; Johnston, K. P.; Sokolov, K. V. Controlled Assembly of Biodegradable Plasmonic Nanoclusters for Near-Infrared Imaging and Therapeutic Applications. *ACS Nano* **2010**, *4*, 2178–2184.
5. Tam, J. M.; Murthy, A. K.; Ingram, D. R.; Nguyen, R.; Sokolov, K. V.; Johnston, K. P. Kinetic Assembly of Near-IR Active Gold Nanoclusters Using Weakly Adsorbing Polymers To Control the Size. *Langmuir* **2010**, *26*, 8988–8999.
6. Xia, Y. S.; Nguyen, T. D.; Yang, M.; Lee, B.; Santos, A.; Podsiadlo, P.; Tang, Z. Y.; Glotzer, S. C.; Kotov, N. A. Self-Assembly of Self-Limiting Monodisperse Supraparticles from Polydisperse Nanoparticles. *Nat. Nanotechnol.* **2011**, *6*, 580–587.
7. Ofir, Y.; Samanta, B.; Rotello, V. M. Polymer and Biopolymer Mediated Self-Assembly of Gold Nanoparticles. *Chem. Soc. Rev.* **2008**, *37*, 1814–1825.
8. Srivastava, S.; Frankamp, B. L.; Rotello, V. M. Controlled Plasmon Resonance of Gold Nanoparticles Self-Assembled with PAMAM Dendrimers. *Chem. Mater.* **2005**, *17*, 487–490.
9. Larson-Smith, K.; Pozzo, D. C. Scalable Synthesis of Self-Assembling Nanoparticle Clusters Based on Controlled Steric Interactions. *Soft Matter* **2011**, *7*, 5339–5347.
10. Wilcoxon, J. P.; Martin, J. E.; Schaefer, D. W. Aggregation in Colloidal Gold. *Phys. Rev. A* **1989**, *39*, 2675–2688.
11. Lu, P. J.; Zaccarelli, E.; Ciulla, F.; Scholfield, A. B.; Sciortino, F.; Weitz, D. A. Gelation of Particles with Short-Range Attraction. *Nature* **2008**, *453*, 499–504.
12. Sedgwick, H.; Egelhaaf, S. U.; Poon, W. C. K. Clusters and Gels in Systems of Sticky Particles. *J. Phys.: Condens. Matter* **2004**, *16*, S4913–S4922.
13. Buitenhuis, J.; Dhont, J. K. G.; Lekkerkerker, H. N. W. Static and Dynamic Light Scattering by Concentrated Colloidal Suspensions of Polydisperse Sterically Stabilized Boehmite Rods. *Macromolecules* **1994**, *27*, 7267–7277.
14. Johnston, K. P.; Maynard, J. A.; Truskett, T. M.; Borwankar, A. U.; Miller, M. A.; Wilson, B. K.; Dinin, A. K.; Khan, T. A.; Kaczorowski, K. J. Concentrated Dispersion of Equilibrium Protein Nanoclusters That Reversibly Dissociate into Active Monomers. *ACS Nano* **2012**, *6*, 1357–1369.
15. Groenewold, J.; Kegel, W. K. Anomalously Large Equilibrium Clusters of Colloids. *J. Phys. Chem. B* **2001**, *105*, 11702–11709.
16. Stradner, A.; Sedgwick, H.; Cardinaux, F.; Poon, W. C. K.; Egelhaaf, S. U.; Schurtenberger, P. Equilibrium Cluster Formation in Concentrated Protein Solutions and Colloids. *Nature* **2004**, *432*, 492–495.
17. Porcar, L.; Falus, P.; Chen, W.-R.; Faraone, A.; Fratini, E.; Hong, K.; Baglioni, P.; Liu, Y. Formation of the Dynamic Clusters in Concentrated Lysozyme Protein Solutions. *J. Phys. Chem. Lett.* **2010**, *1*, 126–129.
18. Weissleder, R. A Clearer Vision for *In Vivo* Imaging. *Nat. Biotechnol.* **2001**, *19*, 316–317.
19. Mallidi, S.; Larson, T.; Aaron, J.; Sokolov, K.; Emelianov, S. Molecular Specific Optoacoustic Imaging with Plasmonic Nanoparticles. *Opt. Express* **2007**, *15*, 6583–6588.
20. Mallidi, S.; Larson, T.; Tam, J.; Joshi, P. P.; Karplouk, A.; Sokolov, K.; Emelianov, S. Multiwavelength Photoacoustic Imaging and Plasmon Resonance Coupling of Gold Nanoparticles for Selective Detection of Cancer. *Nano Lett.* **2009**, *9*, 2825–2831.
21. Agarwal, A.; Huang, S. W.; O'Donnell, M.; Day, K. C.; Day, M.; Ashkenazi, S. Targeted Gold Nanorod Contrast Agent for Prostate Cancer Detection by Photoacoustic Imaging. *J. Appl. Phys.* **2007**, *102*, 0647011–0647014.
22. Khlebtsov, B.; Zharov, V.; Melnikov, A.; Tuchin, V.; Khlebtsov, N. Optical Amplification of Photothermal Therapy with Gold Nanoparticles and Nanoclusters. *Nanotechnology* **2006**, *17*, 5167–5179.
23. Hirsch, L. R.; Stafford, R. J.; Bankson, J. A.; Sershen, S. R.; Rivera, B.; Price, R. E.; Hazle, J. D.; Halas, N. J.; West, J. L. Nanoshell-Mediated Near-Infrared Thermal Therapy of Tumors under Magnetic Resonance Guidance. *Proc. Natl. Acad. Sci. U.S.A.* **2003**, *100*, 13549–13554.
24. Loo, C.; Lowery, A.; Halas, N.; West, J.; Drezek, R. Immunotargeted Nanoshells for Integrated Cancer Imaging and Therapy. *Nano Lett.* **2005**, *5*, 709–711.

25. Larson, T. A.; Bankson, J.; Aaron, J.; Sokolov, K. Hybrid Plasmonic Magnetic Nanoparticles as Molecular Specific Agents for MRI/Optical Imaging and Photothermal Therapy of Cancer Cells. *Nanotechnology* **2007**, 18.
26. von Maltzahn, G.; Park, J.-H.; Agrawal, A.; Bandaru, N. K.; Das, S. K.; Sailor, M. J.; Bhatia, S. N. Computationally Guided Photothermal Tumor Therapy Using Long-Circulating Gold Nanorod Antennas. *Cancer Res.* **2009**, *69*, 3892–3900.
27. Choi, H. S.; Liu, W.; Misra, P.; Tanaka, E.; Zimmer, J. P.; Ipe, B. I.; Bawendi, M. G.; Frangioni, J. V. Renal Clearance of Quantum Dots. *Nat. Biotechnol.* **2007**, *25*, 1165–1170.
28. Gavrilenko, V. I. *Optics of Nanomaterials*; Pan Stanford Publishing: Singapore, 2011; pp 63−66.
29. Zhang, C.; Pansare, V. J.; Prud'homme, R. K.; Priestley, R. D. Flash Nanoprecipitation of Polystyrene Nanoparticles. *Soft Matter* **2012**, *8*, 86–93.
30. Cheng, C.; Wen, Y.; Xu, X.; Gu, H. Tunable Synthesis of Carboxyl-Functionalized Magnetite Nanocrystal Clusters with Uniform Size. *J. Mater. Chem.* **2009**, *19*, 8782–8788.
31. Zaccarelli, E. Colloidal Gels: Equilibrium and Non-equilibrium Routes. *J. Phys.: Condens. Matter* **2007**, *19*, 1–50.
32. Edwards, T. D.; Bevan, M. A. Polymer Mediated Depletion Attraction and Interfacial Colloidal Phase Behavior. *Macromolecules* **2012**, *45*, 585–594.
33. Piech, M.; Walz, J. Y. Direct Measurement of Depletion and Structural Forces in Polydisperse, Charged Systems. *J. Colloid Interface Sci.* **2002**, *253*, 117–129.
34. Kulkarni, A. M.; Chatterjee, A. P.; Schweizer, K. S.; Zukoski, C. F. Depletion Interactions in the Protein Limit: Effects of Polymer Density Fluctuations. *Phys. Rev. Lett.* **1999**, *83*, 4554–4557.
35. Lekkerkerker, H. N. W.; Tuinier, R. *Colloids and the Depletion Interaction*; Springer: New York, 2011; Vol. 833, pp 12−15.
36. Asakura, S.; Oosawa, F. On Interaction between 2 Bodies Immersed in a Solution of Macromolecules. *J. Chem. Phys.* **1954**, *22*, 1255–1256.
37. Asakura, S.; Oosawa, F. Interaction between Particles Suspended in Solutions of Macromolecules. *J. Polym. Sci.* **1958**, *33*, 183–192.
38. Chen, S.; Yu, F.; Yu, Q.; He, Y.; Jiang, S. Strong Resistance of a Thin Crystalline Layer of Balanced Charged Groups to Protein Adsorption. *Langmuir* **2006**, *22*, 8186–8191.
39. Sakai, T.; Alexandridis, P. Mechanism of Gold Metal Ion Reduction, Nanoparticle Growth and Size Control in Aqueous Amphiphilic Block Copolymer Solutions at Ambient Conditions. *J. Phys. Chem. B* **2005**, *109*, 7766–7777.
40. Fresnais, J.; Lavelle, C.; Berret, J.-F. Nanoparticle Aggregation Controlled by Desalting Kinetics. *J. Phys. Chem. C* **2009**, *113*, 16371–16379.
41. Berret, J.-F. Stoichiometry of Electrostatic Complexes Determined by Light Scattering. *Macromolecules* **2007**, *40*, 4260–4266.
42. Ivanova, T.; Panaiotov, I.; Proust, J. E.; Benoit, J. P.; Verger, R. Hydrolysis Kinetics of Poly(D,L-Lactide) Monolayers Spread on Basic or Acidic Aqueous Subphases. *Colloids Surf., B* **1997**, *8*, 217–225.
43. Halas, N. J.; Lal, S.; Chang, W.-S.; Link, S.; Nordlander, P. Plasmons in Strongly Coupled Metallic Nanostructures. *Chem. Rev.* **2011**, *111*, 3913–3961.
44. Gobin, A. M.; Lee, M. H.; Halas, N. J.; James, W. D.; Drezek, R. A.; West, J. L. Near-Infrared Resonant Nanoshells for Combined Optical Imaging and Photothermal Cancer Therapy. *Nano Lett.* **2007**, *7*, 1929–1934.
45. Chen, J.; Saeki, F.; Wiley, B. J.; Cang, H.; Cobb, M. J.; Li, Z. Y.; Au, L.; Zhang, H.; Kimmey, M. B.; Li, X.; *et al.* Gold Nanocages: Bioconjugation and Their Potential Use as Optical Imaging Contrast Agents. *Nano Lett.* **2005**, *5*, 473–477.
46. Song, K. H.; Kim, C.; Cobley, C. M.; Xia, Y.; Wang, L. V. Near-Infrared Gold Nanocages as a New Class of Tracers for Photoacoustic Sentinel Lymph Node Mapping on a Rat Model. *Nano Lett.* **2009**, *9*, 183–188.
47. Huang, X.; El-Sayed, I. H.; Qian, W.; El-Sayed, M. A. Cancer Cell Imaging and Photothermal Therapy in the Near-Infrared Region by Using Gold Nanorods. *J. Am. Chem. Soc.* **2006**, *128*, 2115–2120.
48. Link, S.; Mohamed, M. B.; El-Sayed, M. A. Simulation of the Optical Absorption Spectra of Gold Nanorods as a Function of Their Aspect Ratio and the Effect of the Medium Dielectric Constant. *J. Phys. Chem. B* **1999**, *103*, 3073–3077.
49. Wang, W.; Yang, X.; Cui, H. Growth Mechanism of Flower-like Gold Nanostructures: Surface Plasmon Resonance (SPR) and Resonance Rayleigh Scattering (RRS) Approaches to Growth Monitoring. *J. Phys. Chem. C* **2008**, *112*, 16348–16353.
50. Wang, Z.; Zhang, J.; Ekman, J. M.; Kenis, P. J. A.; Lu, Y. DNA-Mediated Control of Metal Nanoparticle Shape: One-Pot Synthesis and Cellular Uptake of Highly Stable and Functional Gold Nanoflowers. *Nano Lett.* **2010**, *10*, 1886–1891.
51. Nehl, C. L.; Liao, H.; Hafner, J. H. Optical Properties of Star-Shaped Gold Nanoparticles. *Nano Lett.* **2006**, *6*, 683–688.
52. Trigari, S.; Rindi, A.; Margheri, G.; Sottini, S.; Dellepiane, G.; Giorgetti, E. Synthesis and Modelling of Gold Nanostars with Tunable Morphology and Extinction Spectrum. *J. Mater. Chem.* **2011**, *21*, 6531–6540.
53. Rechberger, W.; Hohenau, A.; Leitner, A.; Krenn, J. R.; Lamprecht, B.; Aussenegg, F. R. Optical Properties of Two Interacting Gold Nanoparticles. *Opt. Commun.* **2003**, *220*, 137–141.
54. Chithrani, B. D.; Ghazani, A. A.; Chan, W. C. W. Determining the Size and Shape Dependence of Gold Nanoparticle Uptake into Mammalian Cells. *Nano Lett.* **2006**, *6*, 662–668.
55. Kooi, M. E.; Cappendijk, V. C.; Cleutjens, K. B. J. M.; Kessels, A. G. H.; Kitslaar, P. J. E. H. M.; Borgers, M.; Frederik, P. M.; Daemen, M. J. A. P.; van Engelshoven, J. M. A. Accumulation of Ultrasmall Superparamagnetic Particles of Iron Oxide in Human Atherosclerotic Plaques Can Be Detected by *In Vivo* Magnetic Resonance Imaging. *Circulation* **2003**, *107*, 2453–2458.
56. Aaron, J.; Travis, K.; Harrison, N.; Sokolov, K. Dynamic Imaging of Molecular Assemblies in Live Cells Based on Nanoparticle Plasmon Resonance Coupling. *Nano Lett.* **2009**, *9*, 3612–3618.
57. Khlebtsov, N.; Dykman, L. Biodistribution and Toxicity of Engineered Gold Nanoparticles: A Review of *In Vitro* and *In Vivo* Studies. *Chem. Soc. Rev.* **2011**, *40*, 1647–1671.
58. Xu, L.; Guo, Y.; Xie, R.; Zhuang, J.; Yang, W.; Li, T. Three-Dimensional Assembly of Au Nanoparticles Using Dipeptides. *Nanotechnology* **2002**, *13*, 725–728.
59. Ryoo, W.; Webber, S. E.; Johnston, K. P. Water-in-Carbon Dioxide Microemulsions with Methylated Branched Hydrocarbon Surfactants. *Ind. Eng. Chem. Res.* **2003**, *42*, 6348–6358.
60. Hiemenz, P. C.; Rajagopalan, R. *Principles of Colloid and Surface Chemistry*, 3 ed.; Taylor & Francis: New York, 1997; pp 546−556.